Article

Not peer-reviewed version

Compaction and Pressure Solution of Mixed Mineral Assemblages: Implications for Granite Fracture Sealing in the Near-Field of High-Level Radioactive Waste Repository

Xiao Tian *, Ju Wang *, Jia-Wei Wang, Jing-Li Xie, Zhi-Chao Zhou, Ke Li

Posted Date: 8 May 2026

doi: 10.20944/preprints202605.0540.v1

Keywords: pressure solution; compaction; fracture sealing; granite; mixed mineral assemblages; HLW disposal

 doi:10.20944/preprints202605.0540.v1

Article

Compaction and Pressure Solution of Mixed Mineral Assemblages: Implications for Granite Fracture Sealing in the Near-Field of High-Level Radioactive Waste Repository

Xiao Tian [1,2,*], Ju Wang [1,2,*], Jia-Wei Wang [1,2], Jing-Li Xie [1,2], Zhi-Chao Zhou [1,2] and Ke Li [3]

[1] Beijing Research Institute of Uranium Geology, Beijing 100029, China

[2] CAEA Innovation Center for Geological Disposal of High-Level Radioactive Waste, Beijing 100029, China

[3] School of Resources and Safety Engineering, Chongqing University, Chongqing 400044, China

* Correspondence: wangju2025@briug.cn; tianxiao@briug.cn

Abstract

The sealing behavior of fracture-filling minerals in the near-field of the deep geological repository (DGR) is critical for the safe disposal of high-level radioactive waste (HLW). In granite host rocks, natural fractures are often filled with polymineralic assemblages of calcite, quartz, and clay minerals; however, their coupled compaction–pressure solution mechanisms under thermal–hydraulic–mechanical–chemical (THMC) conditions remain poorly understood. In this study, 12 fracture sealing experiments were conducted on Beishan granite and its typical fracture fillings at 90 °C and 15 MPa effective stress, using different pore fluids and systematically varying grain size (75–250 μm), mineral proportions, and clay content. The results demonstrate that pressure solution–precipitation of calcite in saturated $CaCO_3$ solution is the key mechanism for long-term fracture sealing, achieving a compaction strain of 24.6%—substantially higher than those obtained in deionized water (20.6%) and under dry conditions (14.8%). Fine-grained calcite compacts more effectively than its coarse-grained counterpart, reaching a porosity as low as 4.8%; rigid quartz accelerates calcite pressure solution via stress concentration at grain contacts; and a moderate amount of clay minerals (~20 wt%) further reduces porosity to 2.1% through lubrication and micropore filling. The study reveals a multi-stage process transitioning from mechanical compaction to pressure solution–precipitation, and a synergistic sealing mechanism dominated by calcite compaction–pressure solution, augmented by quartz stress transfer and clay lubrication. These findings revise the traditional monomineralic understanding and provide a scientific basis for safety assessment of HLW disposal and the design of natural sealing materials.

Keywords: pressure solution; compaction; fracture sealing; granite; mixed mineral assemblages; HLW disposal

1. Introduction

The safe disposal of high-level radioactive waste (HLW) constitutes a critical constraint on the sustainable development of nuclear energy. The deep geological repository (DGR), which employ a multi-barrier system to isolate HLW from the biosphere over geological timescales, are internationally recognized as the most technically feasible solution [1–3]. Granite, one of the main host rock types for repositories, possesses inherent advantages such as high strength, low permeability, and low porosity. However, natural fractures within granite continuously evolve under complex geological conditions [4–11], forming potential pathways for groundwater flow and radionuclide migration that compromise the long-term safety of the repository [12,13]. These fractures are commonly filled with natural minerals including calcite, quartz, and clay minerals [14–

 doi:10.20944/preprints202605.0540.v1

16]. Under the coupled thermal–hydraulic–mechanical–chemical (THMC) conditions prevailing in the near-field of repository, these fracture-filling minerals may undergo compaction, dissolution, and precipitation, thereby altering the sealing state of the fractures [8,17–20]. Therefore, elucidating the sealing processes and mechanisms of mineral-filled fractures under coupled THMC conditions is a fundamental issue for both repository safety assessment and the development of natural sealing materials.

Under non-high-temperature and non-high-pressure conditions, achieving true sealing of crystal-mineral-filled natural fractures requires not only physical changes but, more importantly, free-face dissolution–precipitation or pressure solution [21]. Previous studies have extensively investigated the kinetic behavior of compaction, dissolution, and precipitation in monomineralic systems of calcite or quartz [22–27]. Weyl [17] and Tada et al. [18] demonstrated that stress-induced mineral dissolution and compaction mechanisms can lead to progressive rock deformation. Ellis [28] found that increasing pore fluid salinity significantly enhances calcite solubility. Hilgers et al. [29] revealed the accelerating effect of temperature on quartz dissolution–precipitation. Zhang et al. systematically explored the influences of temperature, effective stress, solution chemistry, and grain size on the pressure solution of calcite, demonstrating that the pressure solution strain rate increases with rising temperature and decreasing grain size, whereas specific ions such as Mg^{2+} and HPO_4^{2-} strongly inhibit the pressure solution process [24,26,30]. At the engineering scale of DGR, Rimstidt et al. [31], Dobson et al. [32], and Zhang [33] performed fracture sealing experiments on tuff and clay rock, confirming the potential for mineral precipitation to induce long-term fracture closure. Recent studies indicate that contrasting mechanical and chemical properties of mineral phases in polymineralic systems generate coupled inter-mineral effects. These effects—including stress concentration at rigid–soft contacts, differential dissolution, and clay lubrication—collectively control compaction and sealing behavior [34–36].

Nevertheless, existing studies exhibit notable limitations. First, experimental investigations have largely focused on tuff or clay rock [37]; systematic studies on granite and its typical fracture-filling minerals remain scarce, and direct microstructural evidence accessible to visual observation is lacking. Second, the filling materials employed in experiments have predominantly been monomineralic (e.g., pure calcite or pure quartz). In reality, fracture fillings in granite are typically heterogeneous assemblages of mixed minerals with a broad grain size distribution [2]. Previous studies have not accounted for the mechanical–chemical coupling effects among different mineral phases. These shortcomings, to some extent, constrain the reliability of predictions for the long-term evolution of fracture sealing in the repository near-field.

This study focuses on the critical issue of granite fracture sealing in the near-field of DGR. Taking the Beishan granite and its common fracture-filling minerals as the test samples, a specially designed apparatus capable of simultaneous monitoring of temperature, fluid pressure, stress, and strain was developed. A series of fracture sealing tests were conducted under varying conditions of grain size, mineral composition, and fluid chemistry. The objective is to reveal the sealing processes and mechanisms of mixed-mineral-filled fractures under repository near-field conditions, to provide a critical basis for repository safety assessment, and to lay a theoretical foundation for the development of fracture sealing materials.

2. Sample Collection and Preparation

All rock and mineral materials used in this study were collected from deep boreholes at the Beishan site, the pre-selected candidate area for China's HLW repository. The rock samples consist of fresh granodiorite—the predominant lithology at the site—taken from the 465.6–601.5 m depth of borehole BS49 (core diameter 63 mm). Fracture-filling materials were recovered from 11 boreholes (BS35–BS42 and BSQ29–BSQ31) distributed across the site. These materials are predominantly polymineralic mixtures, dominated by calcite, the most abundant fracture-filling mineral in Beishan granite, together with quartz and clay minerals (mainly smectite) [2,15].

 doi:10.20944/preprints202605.0540.v1

All samples were prepared following specific procedures to meet experimental requirements after collection. The granite core was first cut into 10 cm long columns (Figure 1a), and the outer surfaces were polished flat and smooth to fit the uniaxial pressure cell. A circumferential notch with a cutting depth of approximately 15 mm was then machined at the mid-height of each column. The sample was fractured along this notch by applying a force, forming a natural rough cross-section with a diameter of approximately 30mm as the experimental fracture surface (Figure 1b). Due to the fact that almost all fracture-filling materials collected comprised mixed mineral assemblages, they were hand-picked under a microscope, grinded used a mortar, and screened out pure mineral particles or powders of calcite and quartz with average grain sizes of 75 μm, 150 μm, and 250 μm, respectively, using a nickel wire mesh. Clay minerals were separated and purified by gravity settling and other purification techniques.

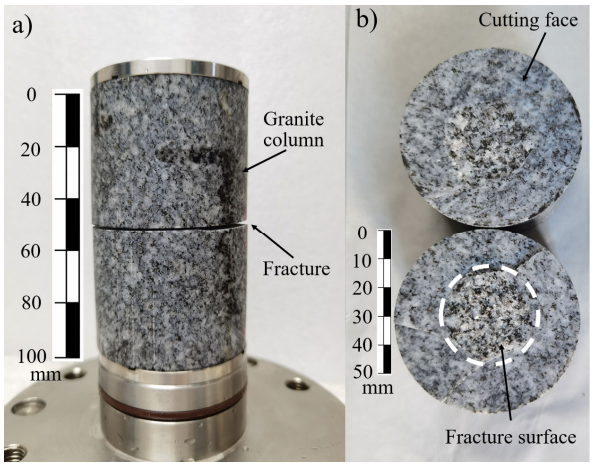

Figure 1. (a) Granite column sample with a fracture, and (b) the rough fracture surface.

The pore fluid employed in the majority of the tests was a saturated $CaCO_3$ solution. This solution was chosen because it maintains a constant ion concentration during testing and becomes supersaturated at elevated temperatures, thereby promoting calcite precipitation and facilitating fracture sealing. The solution was prepared at room temperature by adding excess $CaCO_3$ powder to deionized water and stirring vigorously for approximately 40 h. One set of tests employed deionized water to isolate the contribution of pore fluid chemistry.

3. Test Methodology

3.1. Test Facility

The experimental apparatus, as shown in Figure 2, is built around a custom-designed uniaxial pressure cell comprising a base, a cylindrical chamber, and an upper piston. Fluid inlet and outlet ports are integrated into the base and the piston, respectively. The internal chamber has a cross-sectional diameter of 65 mm to accommodate granite columns of 63 mm diameter. Axial stress is applied by a geotechnical consolidation frame with a maximum loading capacity of 100 kN, transmitted to the sample through a circular loading head equipped with a load cell. Pore fluid pressure is generated and maintained at a constant level by an osmotic pressure–volume controller and delivered into the pressure cell through a high-pressure isolation vessel filled with the prepared solution. Sealing rings are fitted around the piston and the base adjacent to the sample to prevent solution leakage. Grooved metal spacers with a cross-shaped recession were placed at both the top and bottom surfaces of the sample to ensure unimpeded fluid flow. The temperature control system employed an immersion circulator (accuracy ±0.5 °C) operating under closed-loop PID control, with dimethyl silicone oil as the circulating medium. The exterior of the pressure cell was wrapped with insulating wool to minimize heat loss. For data acquisition, a high-precision displacement transducer

 doi:10.20944/preprints202605.0540.v1

(resolution ±1 μm) was mounted between the upper piston and the cell body to continuously record the axial compaction strain of the specimen. Pore pressure transducers (accuracy 0.25%) were installed at the upper and lower fluid ports to monitor the pore fluid pressure. A thermocouple embedded in the base of the pressure cell provided real-time monitoring of the internal temperature. All sensor data were acquired and stored in real time by a data logger running GDSLAB software. The entire apparatus was calibrated against certified reference materials to verify measurement accuracy prior to the tests.

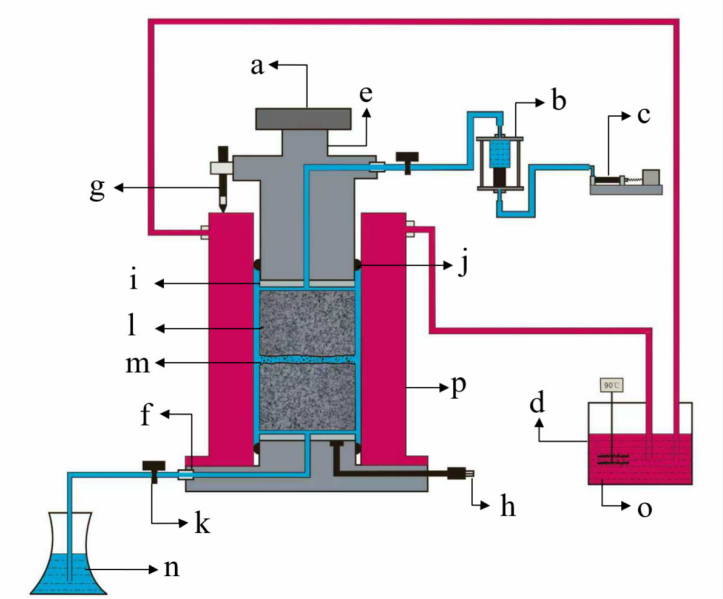

Figure 2. Schematic illustration of the experimental apparatus. (a) pressure loading head, (b) high-pressure isolation vessel, (c) osmotic pressure–volume controller, (d) constant-temperature immersion circulator, (e) axial load cell, (f) pore pressure transducer, (g) displacement transducer, (h) thermocouple, (i) grooved metal spacer, (j) sealing ring, (k) ball valve, (l) granite column, (m) fracture-filling minerals, (n) pore solution, (o) dimethyl silicone oil, (p) uniaxial pressure cell.

3.2. Test Procedure

The designated fracture-filling minerals were homogeneously mixed and spread evenly over the fracture surface, after which the assembled sample was placed into the pressure cell. At the beginning of each test, the fracture-filling material was first pre-compacted under dry conditions by applying an axial stress (σ_a) of 30 MPa for approximately 0.5 h to eliminate purely mechanical effects such as grain rearrangement and to establish a standardized initial microstructure. Subsequently, the axial stress was reduced to 6–8 MPa, and the pore fluid was injected. A constant pore fluid pressure (P_f) of 5 MPa was maintained while the temperature was raised to 90 °C. Once the temperature stabilized, the axial stress was gradually increased to the target value for each group such that the effective stress ($\sigma_e = \sigma_a - P_f$) equaled 15 MPa. Throughout the experiment, the normal displacement across the fracture and other parameters were continuously recorded at intervals of up to 10 min to capture the mineral deformation and fracture sealing progress. The test was terminated once the rate of displacement change became negligible. After each test, the system was cooled and depressurized, and the reacted pore solution was collected through the ball valve. The pressure cell was then disassembled, and the granite column was retrieved, dried, weighed, and subjected to SEM microanalysis. A total of 12 such tests were conducted in this study, each continuously monitored for 9–12 days, yielding a cumulative experimental duration of 138 days.

 doi:10.20944/preprints202605.0540.v1

3.3. Data Analysis

To characterize the degree of fracture sealing, the data analysis focused on the axial compaction strain of the sample, the porosity of the filling material, and its microstructure. The compaction strain (ε_v) directly quantifies the degree of compaction deformation of the filling material under uniaxial stress and is calculated from the displacement transducer data as $\varepsilon_V = \frac{\Delta L}{L_0}$ (Figure 3). The porosity of the mineral filling material indirectly reflects the degree of fracture sealing and was determined from sample measurements using the following formula:

$$\Phi = \frac{V_P}{V_{tot}} = 1 - \frac{w_s}{l\pi r^2 \rho_s} \quad (1)$$

where V_{tot} is the total volume of the filling layer, V_P is the total pore volume within the layer, l is the layer thickness, r is the radius of the fracture surface, W_s is the mass of fracture filling minerals, and ρ_s is the mean density of the minerals, calculated as the weighted average of the mass fractions of the constituent mineral phases.

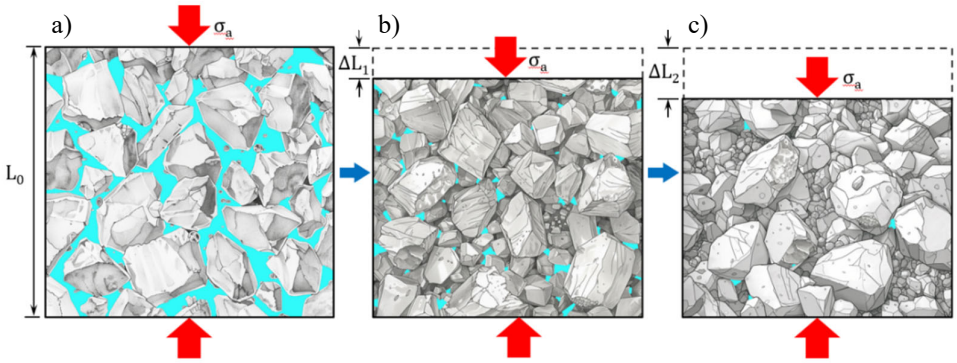

Figure 3. Evolution of compaction strain of the fracture-filling layer. L_0 represents the initial fracture thickness before testing (a). $\Delta L_1/L_0$ represents the vertical strain after pre-compaction (b). $\Delta L_2/L_0$ represents the vertical strain at the end of the test (c). Axial stress (σ_a) is maintained constant throughout the test.

SEM images provided direct evidence of mineral deformation and dissolution–precipitation [38]. Specifically, the porosity of the filling material was derived from representative BSE images through pixel analysis and thresholding using ImageJ software [39]. Additionally, mineral grain sizes were measured and statistically analyzed using the Analyze Particles function of ImageJ.

4. Test Results

Overall, the tests were completed successfully. Compaction strain and porosity virtually exhibited clear systematic variations over time, and microstructural images also provided evidence of mineral compaction and dissolution–precipitation. Despite the limited duration (~300 h per test), the systematic variations in strain and porosity, along with microstructural evidence, suffice to elucidate the governing fracture sealing mechanisms. Detailed test conditions and results are presented in Table 1.

4.1. Compaction Behavior and Multi-Stage Evolution

The evolution of compaction strain for the fracture filling composed of fine-grained calcite particles (mean grain size 75 μm) is presented in Figure 4, where the axial strain ($\Delta L/L_0$) and calculated porosity (ϕ) are compared under three conditions of dry, deionized water, and saturated $CaCO_3$ solution. Based on the change rates of strain and porosity, the mineral deformation process can be divided into three distinct stages of pre-compaction, early stage of solution involvement, and equilibrium-approaching.

 doi:10.20944/preprints202605.0540.v1

· Pre-compaction stage (0–0.5 h)

During the first 0.5 h of the test, the filling material underwent purely rapid mechanical compaction under an axial stress of 30 MPa. This stage was dominated by instantaneous grain rearrangement, accompanied by brittle fracturing of grains at highly stressed contacts. The resulting fragments filled adjacent intergranular voids, triggering further sliding and re-rearrangement. For the fine-grained calcite, this mechanical deformation essentially reached a quasi-static equilibrium within 0.5 h, as indicated by the flattening of the strain curve (Figure 4b). Notably, no pore fluid had yet been injected and the temperature remained at ambient conditions, so chemical processes such as dissolution–precipitation were negligible during this stage.

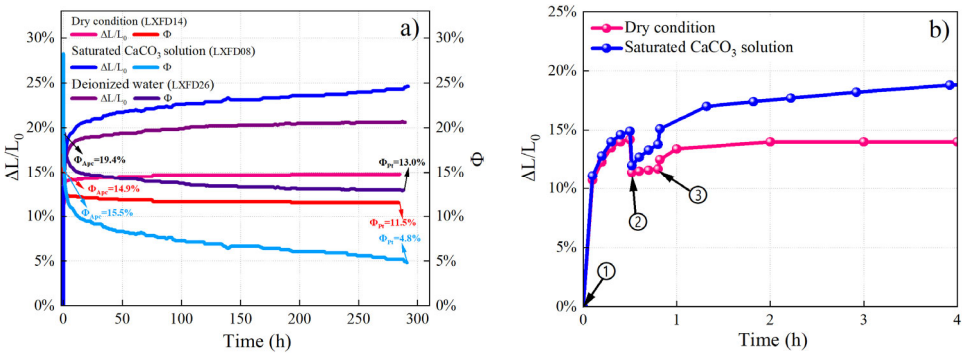

Figure 4. Temporal evolution of compaction strain and calculated porosity of fine-grained calcite samples under saturated $CaCO_3$ solution, deionized water, and dry conditions. (a) the entire test duration; (b) the early stage (0–4 h). Pre-compaction under dry conditions begins at point 1; axial stress is reduced to 6–8 MPa and pore solution is injected at point 2; axial stress is increased to the target value at point 3. Φ_{prec} denotes the porosity after pre-compaction; Φ_{et} denotes the final porosity at the end of the test.

· Early stage of solution involvement (0.5 h to several tens of hours)

Upon injection of the pore fluid and heating to 90 °C, the strain curve displayed a pronounced acceleration in its early phase (Figure 4a). Under saturated $CaCO_3$ solution, the cumulative strain increment from 1 h to 60 h reached 6.8%, corresponding to an average strain rate of 3.2×10^{-7} s^{-1}, while the porosity decreased by 7.4%. This enhanced deformation is mainly attributable to two concurrent mechanisms. Firstly, the liquid phase effectively reduced the friction coefficient at grain contacts that facilitated physical rearrangement. Secondly, the elevated temperature likely enhanced the reactivity of the minerals [40], creating favorable conditions for the onset of chemical processes. In contrast, the dry sample exhibited a considerably slower strain increase, with an average rate of only 2.4×10^{-7} s^{-1} from 1h to 60 h, and its strain increment decayed earlier. This is because its deformation relied entirely on mechanical grain fracturing and rearrangement.

· Equilibrium-approaching stage (after several tens of hours)

After several tens of hours, the strain entered a phase of slow growth accompanied by a gradual decline in porosity, exhibiting a stepwise pattern (Figure 4a). For the sample tested under saturated $CaCO_3$ solution, the strain increases between 221 h and 280 h was merely 0.7%, corresponding to an average strain rate of only 3.3×10^{-8} s^{-1}. This rate is roughly one order of magnitude lower than that in the early stage of solution involvement. The intermittent small "jumps" visible on the strain curve suggest localized restructuring of the grain assembly, likely associated with dissolution at stress concentration positions. Toward the end of the test, the strain curve flattened, indicating that the filling had attained a new quasi-equilibrium granular structure. A comparison of the microstructures after pre-compaction and post-test further reveals marked differences in grain morphology and pore architecture between two stages (Figure 5).

Table 1. Summary of test conditions and results.

Test No.	Duration (h)	Axial pressure (kN)	Fracture surface area (mm^2)	Pore solution	Initially added fracture-filling minerals			Compaction strain ($\Delta L/L_0$)			Porosity(Φ)		
					Thickness (mm)	Mass (g)	Mineral components: average grain size, mass ratio	Apc	Pt	ΔS	Apc	Pt	$\Delta\Phi$
LXFD08	294.6	13.2	660.2	$CaCO_3$	0.7	0.90	CAL: 75μm, 100%	15.1%	24.6%	+9.5%	15.5%	4.8%	-10.7%
LXFD05	270.6	14.3	716.0	$CaCO_3$	0.7	0.98	CAL: 75μm, 80% QTZ: 75μm, 10% CLAY: 10%	13.5%	23.3%	+9.8%	14.0%	3.0%	-11.0%
LXFD09	286.3	11.4	572.3	$CaCO_3$	0.5	0.49	CAL: 150μm, 100%	21.5%	31.9%	+10.4%	19.6%	7.3%	-12.3%
LXFD11	269.4	13.2	660.2	$CaCO_3$	0.7	0.93	CAL: 75μm, 80% CLAY: 20%	13.1%	22.8%	+9.7%	13.0%	2.1%	-10.9%
LXFD12	284.3	13.2	660.2	$CaCO_3$	0.3	0.89	CAL: 75μm, 78% QTZ: 75μm, 22%	12.5%	21.0%	+8.5%	17.4%	8.5%	-8.9%
LXFD15	277.7	16.6	829.2	$CaCO_3$	0.3	0.48	CAL: 75μm, 49% QTZ: 75μm, 51%	10.1%	15.5%	+5.4%	19.9%	14.8%	-5.1%
LXFD21	264.0	18.2	907.5	$CaCO_3$	0.7	1.02	CAL: 250μm, 100%	23.8%	34.1%	+10.3%	22.3%	10.2%	-12.1%
LXFD22	255.8	17.6	881.0	$CaCO_3$	0.8	1.04	CAL: 75μm, 60% QTZ: 75μm, 20% CLAY: 20%	10.6%	16.5%	+5.9%	15.7%	9.8%	-5.9%
LXFD23	268.9	14.4	720.7	$CaCO_3$	0.4	0.92	CAL: 250μm, 50% CAL: 75μm, 50%	16.9%	29.1%	+12.2%	20.0%	6.2%	-13.8%
LXFD24	269.2	13.2	660.2	$CaCO_3$	0.8	1.03	CAL: 75μm, 20% QTZ: 75μm, 80%	7.2%	10.4%	+3.2%	22.1%	19.4%	-2.7%
LXFD26	289.4	12.9	646.6	D-water	0.8	0.97	CAL: 75μm, 100%	14.3%	20.6%	+6.3%	19.4%	13.0%	-6.4%
LXFD14	285.0	9.9	660.2	/	0.4	0.90	CAL: 75μm, 100%	11.4%	14.8%	+3.4%	14.9%	11.5%	-3.4%

Note: The initial effective stress (σ_e) of all tests is 15MPa, the temperature is 90℃. $CaCO_3$—artificially prepared saturated calcium carbonate solution; D-water—deionized water; CAL—calcite; QTZ—quartz; CLAY: clay mineral. Apc—after pre-compaction; Pt—post-test; ΔS—compaction strain variation; $\Delta\Phi$—porosity variation.

 doi:10.20944/preprints202605.0540.v1

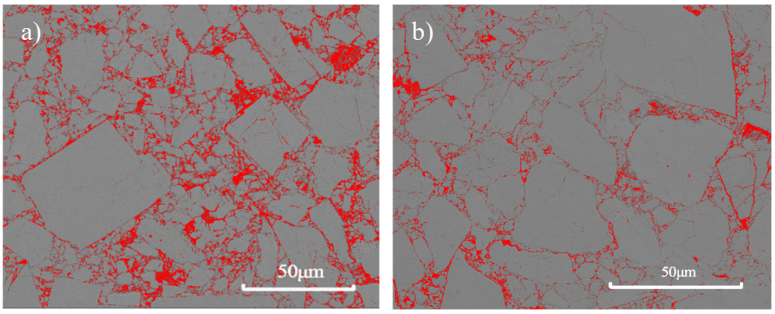

Figure 5. Pore distribution in fracture-filling minerals analyzed from BSE images. The porosity of the fill in sample LXFD08 after pre-compaction (a) and at the end of the test (b) is 15.5% and 4.8%, respectively. Red pixels represent pores; the unified threshold range in ImageJ is 0–100.

Although each test was monitored for nearly 300 h, the slowly increasing strain trend at the end of the tests and the observed microstructures (Figure 5b) indicate that complete compaction and even mutual healing of the mineral grains were not achieved. This observation suggests that natural fracture sealing is a protracted and complex geological process requiring a sufficiently long duration, which is difficult to fully reproduce within the time span accessible to laboratory tests.

4.2. Role of Pore Fluid

A comparison of the results under the three conditions demonstrates that the dry sample entered the quasi-equilibrium state earliest, with a final strain of 14.8%, substantially lower than the 24.6% achieved under saturated $CaCO_3$ solution. The final strain under deionized water (20.6%) fell between these two values. Clearly, purely mechanical compaction can realize only a limited volume reduction. However, the presence of a pore fluid (particularly saturated $CaCO_3$ solution) substantially amplifies the volume loss, likely indicating a fundamental change in the compaction behavior of the filling minerals. SEM images provided direct microscopic evidence for this inference: only grain fracturing and dense packing were observed under dry conditions, whereas mineral dissolution and precipitation were identified under saturated $CaCO_3$ solution (Figure 6). The neoformed precipitates not only filled residual pores but, more importantly, developed intergranular cement with cohesive strength, thereby achieving genuine fracture sealing rather than mere compaction.

 doi:10.20944/preprints202605.0540.v1

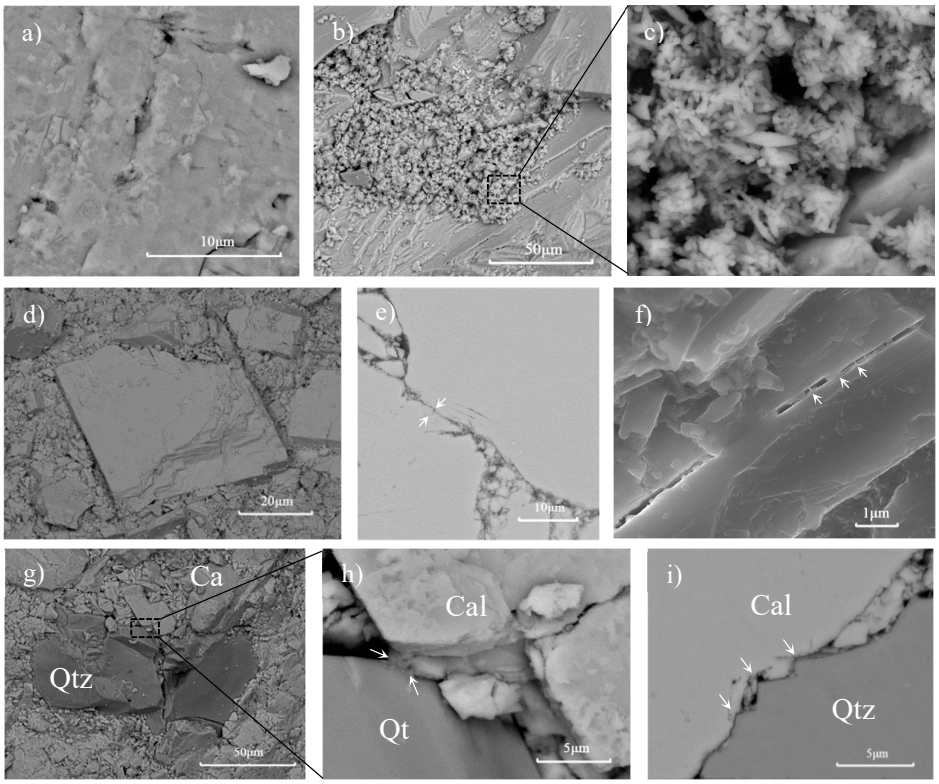

Figure 6. Microstructural evidence of mechanical deformation, dissolution, and re-precipitation of minerals. (a) Dissolution pits and microcracks on a calcite crystal surface, sample LXFD08, BSE image. (b, c) Clusters of fine-grained (1–3 μm) neoformed calcite crystallites precipitated on the sample surface, BSE images. (d) Mechanical fragmentation of calcite particles under dry conditions, sample LXFD14, BSE image. (e) Pressure solution at calcite grain contacts resulting in blurred contact boundaries and local cementation (white arrows), BSE image. (f) A fracture in a calcite crystal with neoformed acicular crystals (white arrows), SEI image. (g, h) Fragmentation and pressure solution at calcite–quartz contacts due to stress concentration (white arrows), sample LXFD12, BSE images. (i) Serrated calcite–quartz contact morphology, with calcite partially crushed into microcrystals filling the contact gap,BSE image.

4.3. Grain-Size Effect

Parallel tests were conducted using calcite particles with mean grain sizes of 75 μm, 150 μm, and 250 μm, together with a bimodal mixture composed of 50wt% 75 μm and 50wt% 250 μm particles, totaling four experimental groups. The results (Figure 7a) show that the fine-grained sample of 75 μm ultimately attained the lowest porosity of only 4.8%, attributable to more efficient particle rearrangement and chemical processes. The samples with different grain sizes exhibited distinct responses at different stages of the tests. The coarse-grained sample of 250 μm displayed a markedly higher strain rate in the early stage, owing to the rapid closure of larger pores between grains during initial compaction. As compaction progressed, the fine-grained sample actually showed a relatively greater porosity reduction, which is closely related to its larger specific surface area and more frequent grain contact. More grain contacts provide more positions of stress concentration, which favor the initiation of pressure solution between minerals.

c)

e)

 doi:10.20944/preprints202605.0540.v1

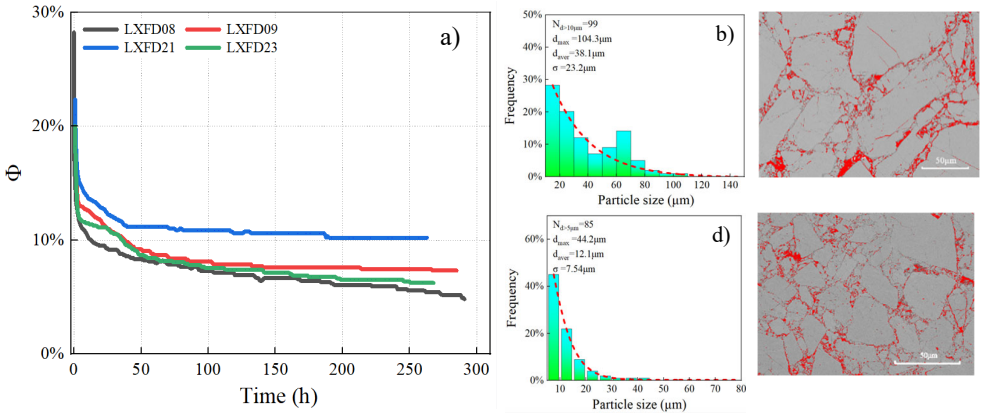

Figure 7. Porosity evolution and post-test grain size distribution of calcite samples with different initial grain sizes. (a) Porosity evolution over time calculated from compaction strain. (b, d) Grain size distribution of the fill after testing in sample LXFD09 and LXFD08. *N*—number of mineral particles; d_{max} and d_{aver}—maximum and average grain size within the statistical range; σ—standard deviation reflecting the degree of size dispersion. (c, e) Pore distribution analyzed from BSE images, with porosities of 7.3% and 4.8%, respectively.

Post-test statistical analysis of grain sizes from SEM images further corroborates these findings (Figure 7b, d). The coarser calcite particles exhibited a broader grain-size distribution after testing, reflecting pronounced fragmentation of calcite particles. Their mean grain size decreased from an initial 150 μm to a final 26.8 μm, with a standard deviation (σ) of 9.13 μm. In contrast, the mean grain size of the fine-grained sample decreased from 75 μm to 12.1 μm with σ = 7.54 μm. A smaller mean grain size implies less intergranular porosity, which benefits the overall sealing performance of the filling material. Additionally, the mineral grains and the intergranular porosity observed in BSE images (Figure 7c, e) further confirm the above interpretation.

4.4. Effects of Mineral Composition

Three groups of samples with identical mean grain size but different calcite-to-quartz mass ratios (4:1, 1:1, and 1:4) were prepared for comparison. The strain curves in Figure 8 show that increasing quartz content resulted in smaller compaction strain and higher final porosity, and vice versa. This pattern indicates that calcite exhibits significantly greater compressibility and brittle–plastic deformability compared to quartz, making it more susceptible to grain deformation and denser packing under identical stress conditions. The presence of quartz significantly restricted the overall compaction of the mixture, owing to its high hardness and low reactivity, which rendered it resistant to mechano-chemical deformation under the temperature and pressure conditions imposed in these tests.

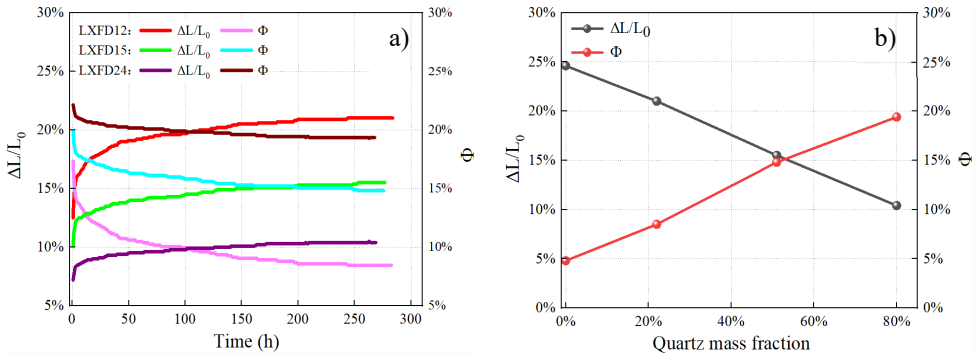

Figure 8. (a) Temporal evolution of compaction strain and porosity for mixed calcite–quartz samples; (b) variation of final strain and porosity as a function of quartz mass fraction.

 doi:10.20944/preprints202605.0540.v1

Notably, in tests using calcite–quartz mixtures as the fill, SEM imaging captured the stress-coupling effect between the two mineral phases (Figure 5g–i). It is virtually certain that quartz grains remained undissolved under the experimental conditions [41]. However, stress concentrations developed significantly at their contacts with calcite, causing preferential fracturing and dissolution of the adjacent calcite surfaces, with calcite re-precipitation subsequently observed near these high-stress positions. The newly precipitated calcite microcrystals effectively filled narrow intergranular voids, which is of critical importance for substantial fracture sealing.

Given that clay minerals (e.g., illite and smectite) are common constituents of fracture fillings in Beishan granite [**], clay minerals were further incorporated into the mixed mineral assemblages at mass fractions of 10% and 20%. Figure 9b–d visually present the mesoscale structural evolution of the same sample with clay addition at different test stages. Under constant axial stress, the mineral grains became progressively more closely packed over time, and the visible fine pores were markedly reduced. From the porosity evolution curves in Figure 9a, the addition of an appropriate amount of clay minerals accelerated the porosity reduction. This is primarily attributed to the intrinsic plasticity and interlayer sliding capability of clay minerals, which facilitated relative sliding and rearrangement of rigid grains and thereby enhanced the overall compaction of the mixture. Among the clay-bearing samples, the mixture containing 20% clay minerals without quartz exhibited the lowest final porosity of 2.1%. However, excessive clay minerals may be mobilized under fluid flow, posing a potential risk to the long-term stability of the fill. These results indicate that moderate clay minerals addition is beneficial for filling intergranular voids, but a balance between porosity reduction and structural stability must be maintained.

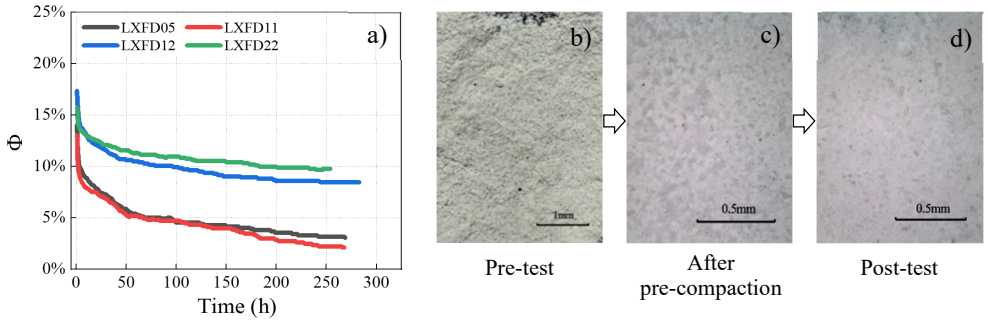

Figure 9. (a) Porosity evolution over time for mixed mineral assemblages containing clay minerals; (b–d) microstructural evolution of sample LXFD22 at different test stages.

5. Discussion

5.1. A Multi-Stage Process: From Mechanical Compaction to Chemo-Mechanical Sealing

The experimental results reveal that sealing of fractures filled with mixed mineral assemblages is a multi-stage process that transitions progressively from purely mechanical compaction to coupled chemo-mechanical sealing. During the initial pre-compaction stage, mineral grains undergo brittle fracturing and instantaneous rearrangement under axial stress, leading to a rapid reduction in porosity. However, this stage produces only dense packing of grains without intergranular cementation possessing cohesive strength, and thus true "sealing" is not achieved. With the involvement of pore fluid and the increase in temperature, the deformation behavior of the fill undergoes a substantive transformation. Fluid lubrication and thermal activation jointly shifted the deformation behavior from purely mechanical to coupled mechanical–chemical, as evidenced by the contrasting strain evolutions under dry and solution-saturated conditions (Section 4.1). The strain evolutions under different solution conditions clearly demonstrate that purely mechanical compaction can achieve only limited volume reduction, and the involvement of a chemically active fluid is the key factor driving effective fracture sealing [42,43]. Especially under saturated $CaCO_3$ solution conditions, numerous minute dissolution pits develop on calcite surfaces, and fine clusters

 doi:10.20944/preprints202605.0540.v1

or needle-shaped crystals precipitate preferentially near grain contacts. These neoformed crystals form cemented structures with cohesive strength between grains, marking the transition from mere volume reduction to true sealing of the fracture.

The above evidence collectively indicates that the driving force of fracture sealing process undergoes a transition from effective-stress-dominated mechanical rearrangement to stress-chemistry-coupled pressure solution and re-precipitation (Figure 10). The latter process not only further reduces porosity but also establishes chemical bonding between grains, providing the fundamental mechanism for long-term effective fracture sealing. Since the temperature and hydrochemical conditions in the repository near-field cannot be maintained at these experimental levels over geological timescales, this coupled chemo-mechanical process in natural settings will span a considerably longer duration than in the laboratory, and the fracture sealing process is likely more complex.

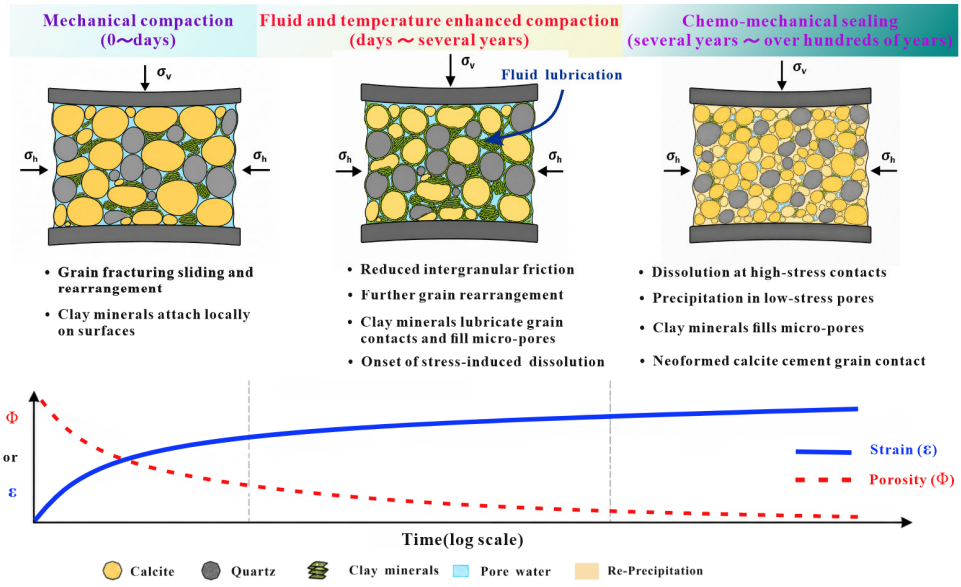

Figure 10. Conceptual model of the multi-stage deformation process of mixed mineral assemblages in granite fractures under DGR near-field conditions.

5.2. Contrasting Mechanical and Chemical Behaviors of Mineral Phases in Mixed Assemblages

The experimental results highlight a fundamental characteristic of mixed mineral assemblages. Different mineral phases exhibit markedly contrasting mechanical responses and chemical reactivities under identical thermal–hydraulic–mechanical–chemical conditions [44], and generate complex coupling effects through inter-mineral interactions.

Calcite displays pronounced dual mechanical–chemical behavior under the experimental conditions. Mechanically, its low hardness imparts considerable brittle–plastic deformability, allowing it to accommodate volume reduction through grain fracturing, sliding, and rearrangement [45,46]. Chemically, the enhanced solubility of calcite at stress concentration positions is the dominant factor driving the pressure solution process [47]. Moreover, these tests have confirmed that pressure solution and re-precipitation of calcite is the key process driving fracture sealing.

In striking contrast, quartz exhibits high rigidity and chemical inertness under the experimental conditions (T=90 °C, $\sigma_e \leq 30$ MPa), resisting its deformation, dissolution, and precipitation [48]. However, the high stiffness of quartz facilitates stress concentrations at quartz–calcite contacts, thereby elevating the local chemical potential in these regions and promoting the initiation and development of calcite pressure solution [35,49]. This demonstrates that rigid quartz does not merely play a passive role in limiting compaction. Instead, a moderate amount of quartz in the mixed mineral

 doi:10.20944/preprints202605.0540.v1

assemblage functions as a stress amplifier. Specifically, quartz grains convert the macroscopic axial stress into locally intensified stresses acting on calcite contacts, thereby indirectly promoting compaction. This finding revises the previous understanding derived from monomineralic systems, that is, a small amount of rigid minerals does not necessarily impair the self-sealing capacity of fractures. On the contrary, such minerals may accelerate local mineral dissolution and re-precipitation through stress transfer, thereby enhancing fracture sealing to a certain degree.

Clay minerals play a distinctive role in the mixed filling system. Their layered structure and low shear strength enable them to act as a lubricant for crystalline grain rearrangement, accelerating volume reduction of the mixed fill by filling intergranular voids and promoting grain sliding [34]. However, this contribution is likely rather limited. When the clay content exceeds a critical limit, excessive fine clay particles may be mobilized and removed under fluid flow, compromising the overall stability of the fill.

In summary, the sealing behavior of mixed-mineral-filled fractures in Beishan granite is primarily governed by the mechanical compaction and dissolution–precipitation of calcite. It should not be overlooked that stress transfer dominated by quartz and lubrication and pore-filling by clay minerals also play positive roles. The dynamic coupling of these mechanisms in time and space collectively determines fracture sealing and its long-term evolution.

5.3. Implications for the Long-Term Sealing of Granite Fractures in HLW Repositories

The experimental results and mechanistic insights gained from this study provide several implications for evaluating the long-term sealing of granite fractures in the near-field of DGR. An important insight is that the tests have confirmed that filled calcite pressure solution and re-precipitation under saturated $CaCO_3$ solution is the core mechanism for long-term fracture sealing. However, the sealing process in granite fractures is likely to be considerably slower than that in claystone fractures. Previous studies have shown that fractures in claystone can achieve a substantial reduction in permeability within months to years under THM conditions [33], benefiting from the inherent plasticity and swelling capacity of clay minerals that enable efficient fracture filling [50,51]. In contrast, the fracture fillings in granite are dominated by crystalline minerals with limited plasticity, with the sealing rate governed mainly by temperature, pressure and solution chemistry. This implies that once the groundwater chemistry in the repository near-field deviates from specific conditions (e.g., $CaCO_3$ saturation), the fracture sealing efficiency is likely to be substantially reduced. Therefore, the long-term evolution of fluid chemistry may become a key factor in predicting fracture sealing performance during safety assessment of HLW disposal.

The influence of mineral heterogeneity on fracture sealing is not determined by a single factor but is instead governed by mechanical–chemical coupling. This study demonstrates that the relative proportions of different mineral phases are a key factor controlling fracture sealing behavior in mixed filled-mineral systems. An excessive rigid component reduces overall compaction, an insufficient reactive component limits the contribution of pressure solution and re-precipitation, and the lubrication and pore-filling effects of clay minerals likewise exhibit an optimal threshold. This balance of proportions also regulates local stress transfer and solute transport pathways, which is crucial for determining effectiveness of long-term fracture sealing. This insight suggests that the mineral assemblage of natural fracture fillings should be incorporated into repository safety assessment frameworks. Predictive models of fracture sealing should also incorporate parameters such as the mass ratio and spatial distribution of filling minerals to improve the reliability of fracture evolution predictions.

At the engineering application level, these findings offer optimization directions for the design of fracture sealing materials. An ideal natural sealing material should possess the following characteristics: (1) the mineral constituents are those naturally occurring in host rock fractures, thereby avoiding drastic alterations to the hydrochemical environment caused by foreign materials, which is critical for radionuclide migration and waste container corrosion; (2) compressible and chemically reactive crystalline minerals (e.g., calcite) serve as the main body to ensure the dominant

 doi:10.20944/preprints202605.0540.v1

contributions of mechanical compaction and mineral precipitation, with a moderate addition of rigid components (e.g., quartz) to accelerate pressure solution through stress transfer; (3) clay minerals are added in appropriate amounts with strictly controlled proportions to exploit their lubrication and void-filling functions while avoiding the risk of loss under fluid flow.

However, the coupled THMC conditions in the repository near-field are, in fact, far more complex than those in laboratory experiments. Factors such as the long-term evolution of temperature gradients and the stress state, and the spatial heterogeneity of fluid chemistry may all exert non-negligible effects on the fracture sealing process [52–54]. It is necessary to conduct larger-scale in-situ tests in the underground research laboratory (URL) to collect long-term monitoring data that better consistent with real geological conditions, and to develop numerical models capable of describing the coupled compaction–pressure solution processes of multiple mineral phases. Only in this way can more reliable data and theoretical tools be provided for the engineering application of HLW repositories.

6. Conclusions

This study elucidates the sealing processes and mechanisms of mixed-mineral-filled fractures in granite under repository near-field conditions through a series of tests. The results demonstrate that the fracture sealing is a multi-stage process transitioning from mechanical compaction to chemo-mechanical sealing. Under the coupled effects of temperature, stress, and saturated $CaCO_3$ solution, calcite undergoes pressure solution and re-precipitation, with neoformed microcrystals cementing grain contacts. This constitutes the key mechanism for achieving true sealing of the mineral-filled fractures. More importantly, mineral heterogeneity is not a detrimental factor for fracture sealing; rather, the coupling effects among mixed mineral phases can enhance the sealing effectiveness. The high compressibility and dissolution-precipitation reactivity of calcite play a dominant role, rigid quartz accelerates calcite pressure solution through stress concentration at grain contacts, and moderate amounts of clay minerals lubricate grain interfaces and fill micropores.

These findings provide a theoretical basis for evaluating the long-term evolution of fracture sealing in mixed mineral assemblages, and lay a foundation for the engineering application of natural fracture sealing materials. Future work will involve in-situ tests at the Beishan URL, coupled with numerical modeling of multiple mineral phase interactions, to provide theoretical tools for the long-term assessment of fracture sealing at the engineering scale.

Author Contributions: Xiao Tian: Supervision, Writing—Review & Editing, Resources, Conceptualization, Methodology. Ju Wang: Project administration, Supervision, Resources, Conceptualization, Methodology. Jia-Wei Wang: Methodology, Validation, Formal analysis. Jing-Li Xie: Data Curation, Investigation. Zhi-Chao Zhou: Data Curation, Resources. Ke Li: Data Curation, Investigation. All authors reviewed and approved the final version of the manuscript.

Funding: This work was financially supported by the China Atomic Energy Authority (CAEA) through the Geological Disposal Program (FZ2101), CAEA Innovation Center for Geological Disposal of High-Level Radioactive Waste (CXJJ2110).

Data Availability Statement: We encourage all authors of articles published in MDPI journals to share their research data. In this section, please provide details regarding where data supporting reported results can be found, including links to publicly archived datasets analyzed or generated during the study. Where no new data were created, or where data is unavailable due to privacy or ethical restrictions, a statement is still required. Suggested Data Availability Statements are available in section “MDPI Research Data Policies” at https://www.mdpi.com/ethics.

Acknowledgments: The authors have reviewed and edited the output and take full responsibility for the content of this publication.

Conflicts of Interest: The authors declare no conflicts of interest.

 doi:10.20944/preprints202605.0540.v1

Abbreviations

The following abbreviations are used in this manuscript:

HLW	High-level Radioactive Waste
THMC	Thermos–hydro–mechanical–chemical
URL	Underground Research Laboratory
DGR	Deep Geological Repository

References

1. Wang, J. Key scientific challenges in geological disposal of high level radioactive waste. **2008**.
2. Wang, J.; Chen, L.; Su, R.; Zhao, X. The Beishan underground research laboratory for geological disposal of high-level radioactive waste in China:Planning, site selection,site characterization and in situ tests. *Journal of Rock Mechanics and Geotechnical Engineering* **2018**, *10*, 411-435.
3. Ojovan, M.I.; Steinmetz, H.J. Approaches to disposal of nuclear waste. *Energies* **2022**, *15*, 7804.
4. YAN, B.-q.; REN, F.-h.; CAI, M.-f.; GUO, Q.-f.; QIAO, C. A review of the research on physical and mechanical properties and constitutive model of rock under THMC multi-field coupling. *Chinese Journal of Engineering* **2020**, *42*, 1389-1399.
5. Wang, J.; Ahmed, B.; Huang, J.; Nong, X.; Xiao, R.; Abbasi, N.S.; Alidekyi, S.N.; Li, H. Physical and mechanical properties and constitutive model of rock mass under THMC coupling: a comprehensive review. *Applied Sciences* **2025**, *15*, 2230.
6. Wang, B.; Liu, Z.; Chen, L.; Ma, H.; Lu, B.; Jian, S.; Du, X. Analysis and layout parameter optimization study for high-level radioactive waste disposal units in granite host rock. *Tunnelling and Underground Space Technology* **2026**, *171*, 107474.
7. Wang, Q.; Lei, K.; Zhu, Z.; Zhang, A. A review of multiphysics coupling numerical modeling techniques for risk assessment in geological disposal of high-level radioactive waste. *Journal of environmental radioactivity* **2026**, *293*, 107902, doi:10.1016/j.Jenvrad.2026.107902.
8. Li, N.; Duan, X.; Wang, J.; Cheemaa, N.; Nazish, H.T.; Peng, G. Bentonite and its modified derivatives: Application and factors influencing radioactive nuclide adsorption. *Progress in Nuclear Energy* **2026**, *191*, 106104.
9. Wang, J.-W.; Wang, J.; Tian, X.; Zhou, Z.; Zhang, J.; Li, N.; Wang, B.; Duan, X. Enhancing barriers for high-level radioactive waste: The role of microbially induced calcium carbonate precipitation in ecological sustainability. *Renewable and Sustainable Energy Reviews* **2026**, *229*, 116666.
10. Chang, C.; Nakagawa, S.; Dong, W.; Zheng, L. Coupled Thermo-Hydrological-Mechanical-Chemical Behavior of Anisotropic Granite for Geologic Disposal of High-Level Radioactive Waste: A Core-Scale Laboratory Investigation. *Rock Mechanics and Rock Engineering* **2025**, 1-15.
11. Li, N.; Duan, X.; Cheemaa, N.; Nazish, H.T.; Peng, G. Stability and transformation of neptunium (Np) species under geological disposal conditions of high-level radioactive waste (HLW). *Journal of Contaminant Hydrology* **2025**, 104739.
12. Tian, X.; Wang, J.; Wang, J.-W. Review on the study of fracture closure behavior in host rock for high-level radioactive

waste disposal. *World Nuclear Geoscience* **2024**, *41*, 1226-1234.

13. Wang, J. On area-specific underground research laboratory for geological disposal of high-level radioactive waste in China. *Journal of Rock Mechanics and Geotechnical Engineering* **2014**, *6*, 99-104.
14. Tian, X.; Wang, J.; Jin, Y.; Li, J. The Isotopic Geochemistry of Filling Calcite in Jiujiang and Xinchang Granite in the Beishan Site for High-Level Radioactive Waste Disposal. *Uranium Geology* **2014**, *30*, 23-29.
15. Wang, J.-W.; Wang, J.; Tian, X.; Duan, X.; Cheemaa, N.; Nazish, H.T. Key geological, mineralogical, and geochemical evidence for the sealing properties of the F34-1 fracture zone in the Xinchang, Beishan and its implications for high-level radioactive waste disposal. *China Geology*, 1-29.
16. Zeng, W.; Wu, Y.; Hu, L.; Li, X.; Huang, Z.; Zhao, P.; Lin, J.; Yu, J. Micro-mechanisms of temperature-dependent triaxial strength in Beishan granite and implications for high-level radioactive waste disposal. *Scientific Reports* **2025**, *15*, 38092.

 doi:10.20944/preprints202605.0540.v1

17. Weyl, P.K. Pressure solution and the force of crystallization: a phenomenological theory. *Journal of geophysical research* **1959**, *64*, 2001-2025.
18. Tada, R.; Maliva, R.; Siever, R. A new mechanism for pressure solution in porous quartzose sandstone. *Geochimica et Cosmochimica Acta* **1987**, *51*, 2295-2301.
19. Llana-Fúnez, S.; Wheeler, J.; Faulkner, D.R. Metamorphic reaction rate controlled by fluid pressure not confining pressure: implications of dehydration experiments with gypsum. *Contributions to Mineralogy and Petrology* **2012**, *164*, 69-79.
20. Putnis, A. Fluid–mineral interactions: Controlling coupled mechanisms of reaction, mass transfer and deformation. *Journal of Petrology* **2021**, *62*, egab092.
21. Ruiz-Agudo, E.; Putnis, C.; Putnis, A. Coupled dissolution and precipitation at mineral–fluid interfaces. *Chemical Geology* **2014**, *383*, 132-146.
22. Rutter, E.; Elliott, D. The Kinetics of Rock Deformation by Pressure Solution (and Discussion), Philos. T. Roy. Soc. A, 283, 203–219. **1976**.
23. Gratier, J.-P.; Dysthe, D.K.; Renard, F. The role of pressure solution creep in the ductility of the Earth's upper crust. *Advances in geophysics* **2013**, *54*, 47-179.
24. Zhang, X.; Salemans, J.; Peach, C.; Spiers, C. Compaction experiments on wet calcite powder at room temperature: Evidence for operation of intergranular pressure solution. **2002**.
25. Zhang, X.; Spiers, C.J.; Peach, C.J. Compaction creep of wet granular calcite by pressure solution at 28 C to 150 C. *Journal of Geophysical Research: Solid Earth* **2010**, *115*.
26. Zhang, X.; Spiers, C. Compaction of granular calcite by pressure solution at room temperature and effects of pore fluid chemistry. *International Journal of Rock Mechanics and Mining Sciences* **2005**, *42*, 950-960.
27. Renard, F.; Røyne, A.; Putnis, C.V. Timescales of interface-coupled dissolution-precipitation reactions on carbonates. *Geoscience Frontiers* **2019**, *10*, 17-27.
28. Ellis, A. The solubility of calcite in sodium chloride solutions at high temperatures. *American Journal of Science* **1963**, *261*, 259-267.
29. Hilgers, C.; Tenthorey, E. Fracture sealing of quartzite under a temperature gradient: Experimental results. *Terra Nova* **2004**, *16*, 173-178.
30. Zhang, X.; Spiers, C.; Peach, C. Effects of pore fluid flow and chemistry on compaction creep of calcite by pressure solution at 150 C. *Geofluids* **2011**, *11*, 108-122.
31. Rimstidt, J.D.; Newcomb, W.D.; Shettel, D.L. A vertical thermal gradient experiment to simulate conditions in vapor dominated geothermal systems, epithermal gold deposits, and high level radioactive repositories in unsaturated media. In *Water-Rock Interaction (WRI-6)*; CRC Press: 2026; pp. 585-588.
32. Dobson, P.F.; Kneafsey, T.J.; Sonnenthal, E.L.; Spycher, N.; Apps, J.A. Experimental and numerical simulation of dissolution and precipitation: implications for fracture sealing at Yucca Mountain, Nevada. *Journal of Contaminant Hydrology* **2003**, *62*, 459-476.
33. Zhang, C.-L. Sealing of fractures in claystone. *Journal of Rock Mechanics and Geotechnical Engineering* **2013**, *5*, 214-220.
34. Niemeijer, A. Velocity-dependent slip weakening by the combined operation of pressure solution and foliation development. *Scientific Reports* **2018**, *8*, 4724.
35. Hu, M.; Steefel, C.I.; Rutqvist, J.; Gilbert, B. Microscale THMC modeling of pressure solution in salt rock: impacts of geometry and temperature. *Rock Mechanics and Rock Engineering* **2023**, *56*, 7071-7089.
36. Wheeler, J. A unifying basis for the interplay of stress and chemical processes in the Earth: support from diverse experiments. *Contributions to Mineralogy and Petrology* **2020**, *175*, 116.
37. Madsen, F. Clay mineralogical investigations related to nuclear waste disposal. *Clay minerals* **1998**, *33*, 109-129.
38. Tulley, C.; ten Thij, L.; Niemeijer, A.; Hamers, M.; Fagereng, Å. Activation of dissolution-precipitation creep causes weakening and viscous behavior in experimentally deformed antigorite. *Journal of Geophysical Research: Solid Earth* **2024**, *129*, e2024JB029053.
39. Shi, X.; Misch, D.; Vranjes-Wessely, S. A comprehensive assessment of image processing variability in pore structural investigations: Conventional thresholding vs. machine learning approaches. *Gas Science and Engineering* **2023**, *115*, 205022.

 doi:10.20944/preprints202605.0540.v1

40. Bai, J.; Li, W.; Li, C.-z.; Bai, Z.; Li, B. Influences of minerals transformation on the reactivity of high temperature char gasification. *Fuel Processing Technology* **2010**, *91*, 404-409.
41. Schepers, A.; Milsch, H. Dissolution–precipitation reactions in hydrothermal experiments with quartz–feldspar aggregates. *Contributions to Mineralogy and Petrology* **2013**, *165*, 83-101.
42. Wang, W.; Tian, Y. Study on Self-Healing and Sealing Technology of Fractured Geothermal Reservoir. *Processes* **2025**, *13*, 3817.
43. Lin, C.; Taleghani, A.D.; Kang, Y.; Xu, C. A coupled CFD-DEM simulation of fracture sealing: Effect of lost circulation material, drilling fluid and fracture conditions. *Fuel* **2022**, *322*, 124212.
44. Mo, C.; Zhao, J.; Zhang, D. Real-time measurement of mechanical behavior of granite during heating–cooling cycle: a mineralogical perspective. *Rock Mechanics and Rock Engineering* **2022**, *55*, 4403-4422.
45. Luo, C.; Yang, X.; Li, J. Mechanical properties of single-crystal calcite and their temperature and strain-rate effects. *Materials* **2022**, *15*, 4613.
46. Zhou, X.; Chen, Q.; Tang, X.; He, R.; Yan, Z.; Xiong, J.; Zhou, Y.; Li, L. Effects of temperature, pressure, and hydration on the microstructural characteristics and mechanical properties of calcite. *Frontiers in Chemistry* **2025**, *13*, 1568585.
47. Croizé, D.; Renard, F.; Bjørlykke, K.; Dysthe, D.K. Experimental calcite dissolution under stress: Evolution of grain contact microstructure during pressure solution creep. *Journal of Geophysical Research: Solid Earth* **2010**, *115*.
48. Zhan, L.; Wang, Q.; Ku, J.; Shang, H.; Shen, Z. Purification technologies for high-purity quartz: From mineralogy to applications. *Separation & Purification Reviews* **2026**, *55*, 209-226.
49. Choi, J.-H.; Seo, Y.-S.; Chae, B.-G. A study of the pressure solution and deformation of quartz crystals at high pH and under high stress. *Nuclear Engineering and Technology* **2013**, *45*, 53-60.
50. El-Zein, A.; Airey, D.; Yu, B.; Esgandani, G.A.; Proust, G.; Dias-da-Costa, D.; Gao, Y.; Gan, Y.; Chen, S. Self-repair of cracks and defects in clay: a review of evidence, mechanisms, theories and nomenclature. *Acta Geotechnica* **2021**, *16*, 3741-3760.
51. Wagner, J.-F. Mechanical properties of clays and clay minerals. In *Developments in clay science*; Elsevier: 2013; Volume 5, pp. 347-381.
52. Samper, J.; Mon, A.; Montenegro, L. Reactive transport model of the long-term geochemical evolution in a HLW repository in granite at the disposal cell scale: Variants, sensitivities, and model simplifications. *Applied Geochemistry* **2024**, *175*, 106188.
53. Zheng, L.; Rutqvist, J.; Xu, H.; Birkholzer, J.T. Coupled THMC models for bentonite in an argillite repository for nuclear waste: Illitization and its effect on swelling stress under high temperature. *Engineering geology* **2017**, *230*, 118-129.
54. Ogata, S.; Yasuhara, H.; Kinoshita, N.; Kishida, K. Coupled thermal–hydraulic–mechanical–chemical modeling for permeability evolution of rocks through fracture generation and subsequent sealing. *Computational Geosciences* **2020**, *24*, 1845-1864.